Development Methodologies for Formula One Aerodynamics

Atsushi OGAWA* Shujiro YANO* Susumu MASHIO*
Takashi TAKIGUCHI* Shinsuke NAKAMURA* Mitsuru SHINGAI*

ABSTRACT

The greater part of aerodynamics development for Formula One involves optimization using objective functions of downforce and the lift-drag ratio (L/D), and verification of effects using wind tunnels and CFD in the development process. As examples of development methodologies used to advance this optimization process, this paper will discuss aerodynamics development tools, including wind tunnels and CFD, and the conventional development indices that employed these tools. In addition, the paper will introduce new indices for analysis of the effect of tire deformation on the aerodynamic load and analysis of transient aerodynamic characteristics during deceleration, and will also consider the findings made regarding air flows using these indices.

1. Introduction

Downforce can be used to increase the side-force limit on the tires when the vehicle is cornering and the braking-force limit when the vehicle is decelerating. Air resistance is an important factor in determining the acceleration performance of the vehicle. The front-rear downforce balance also contributes to vehicle stability. The purpose of aerodynamics development is to maximize either downforce or lift-drag ratio with consideration of the trade-off between these three elements.

During the development process, the vehicle shape was optimized using a 50% scale model in wind tunnel tests, following which effects were verified using full-scale wind tunnel tests. Simultaneous analysis of aerodynamic phenomena using CFD and particle image velocimetry (PIV) helped to enable the development in the model-scale wind tunnel to move forward in an efficient manner. It also became possible to a certain extent to quantitatively evaluate aerodynamic load using CFD, making it a tool capable of supporting part of the optimization process. The importance of CFD is also increasing as a bridge between wind tunnel tests and the vehicle actually running on a race track. For example, using CFD to reproduce the air flow when the tires were deformed by side force, which could not be reproduced using an actual vehicle in a wind tunnel, produced new findings regarding the air flow around the vehicle running on a race track. Some of these findings were verified in wind tunnel tests.

In recent years, attention is beginning to be directed towards unsteady aerodynamic characteristics when the vehicle is vibrating or decelerating. In Formula One, the maximum deceleration force reaches 5 G during braking, and transient aerodynamic characteristics were frequently an issue during deceleration. It was possible, however, to elucidate the effects of some transient aerodynamic phenomena by means of slow-motion tests in water towing tanks.

2. Aerodynamics Development Tools

This chapter will discuss moving-belt wind tunnel equipment and CFD as aerodynamics development tools.

2.1. The Wind Tunnel

2.1.1. Wind tunnel configuration

The Formula One aerodynamics development process generally used a low speed closed circuit wind tunnel. Open and closed test sections were employed. When closed sections were employed, adaptive walls were used to reduce blockage.

When a boundary layer formed on the floor of the wind tunnel, this boundary layer would sometimes separate prior to the boundary layer underneath the vehicle, due to the adverse-pressure gradient underneath the vehicle. The following countermeasures were put into place to address this issue (Fig. 1).

First, knife-edge and perforated-plate structures were used at the inlet of the test section to remove the boundary layers on the floor. Additionally, downstream

* Automobile R&D Center

from these structures, a moving belt was used to control the occurrence of boundary layers. As a result, ground surface boundary layers were not built above the limit height (approximately 3 mm) of the boundary layer pitot rake measurement, and the free stream was confirmed to be maintained.

To help ensure that the belt was not lifted by the low pressure under the vehicle, suction was applied from underneath the belt when a plastic belt was used, and a tensile force was applied between the front and rear drive shafts when a stainless steel belt was used.

In order to minimize the minute deformation of the different parts of the model when aerodynamic loads were applied, the effect of expansion and contraction of materials due to temperature, and temperature drift in measurement devices, the temperature at the test section was maintained at a constant level during tests. For 50% model tests, the temperature was held at 25˚ C, and a wind speed of approximately 45 m/s was used during the optimization process.

2.1.2. Configuration of wind tunnel models and measurement instruments

This section will first discuss the basic configuration of a 50% model (Fig. 2). The model was supported by a strut from the ceiling. The lower section of the strut was fitted with a pivot to help enable the orientation of the model to be changed, an actuator, and a six-component load cell to measure the aerodynamic load on the model.

The spine (framework) of the model was covered by a replaceable bodywork. The front and rear of the spine were fitted with laser ride-height sensors, to control pitch angle and vehicle height. Three-component load cells were positioned at the bases of the front wings (FW) and the rear wings (RW) to measure downforce, drag, and pitching moment.

The model was also fitted with yaw-, roll-, and steer-control mechanisms, for the reproduction of complex vehicle orientations. In addition, the entire floor of the wind tunnel, including the moving belt, was capable of yaw rotation. The model was also fitted with anemometers at the radiator (vane anemometers or differential pressure gauges), pressure scanners to measure the static pressure at each part, and single-axis load cells able to measure the drag on each wheel. The wheel support method is discussed below.

Two types of wheel support were available: wheel-off and wheel-on. In the wheel-off configuration, the wheels were supported by wheel support arms from outside. The wheels were not in contact with the model, and changes in ride height, therefore, did not generate a reaction force in the model. However, slight inaccuracies remained in geometries, including infinitesimal changes in the camber of the wheels, and the distance between the inner faces of the wheels and the adjacent vehicle parts. The wheel-on configuration used a suspension system with the same geometry as an actual vehicle. The suspension was specially designed not to constrain the motion of the pushrod, and could therefore remove a reaction force from the ground. However, bump and rebound of the suspension would produce a slight amount of friction and a spring force which results in a reaction force to the model and for this reason care was necessary on corrections of the zero point (tare measurements) of the measurement devices.

Formerly, rigid tires with trapezoidal cross-sections (manufactured from aluminum or CFRP) which reproduced the squashed shape close to the contact patch around their entire circumferences were employed. More recently, however, it has become standard practice to use 50% scale rubber tires provided by tire suppliers for wind tunnel model use.

Tare measurements were normally conducted while rotating the belt at a low speed, with a wind speed of zero. Reproducing all the vehicle orientations that were to be measured and taking tare measurements at each measurement point during this process would help enable more accurate measurements. However, this method was disadvantageous in terms of measurement time. In many cases therefore, measurement time was reduced by taking one vehicle orientation as representative for tare measurements, or multiplying by the linear approximation of the ride height at this representative orientation and the highest and lowest ride heights.

2.1.3. Flow visualization techniques

PIV measurements were conducted with the technical assistance of the Honda Fundamental Technology Research Center. This section will discuss the set-up for three-dimensional PIV measurements.

A seeding device was positioned behind a heat exchanger, in a space between flow-smoothing honeycombs. The seeding particles were glycol-based, and had a diameter of 1 micrometer. The laser optical system, situated outside the path of the wind, illuminated the periphery of the model. By changing the path of the optical system and the position of the cameras, it was

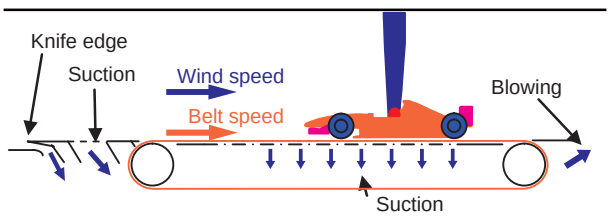

Fig. 1 Moving belt configuration

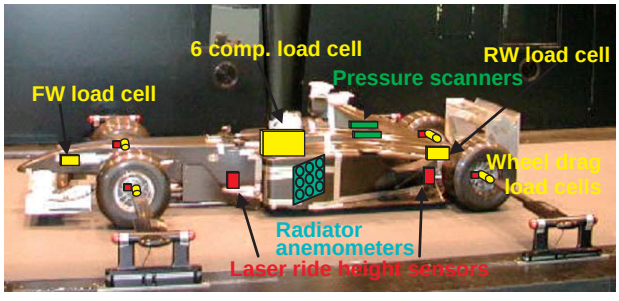

Fig. 2 50% model measurement system

possible to take measurements in the x, y, and z directions (Fig. 3). However, there were limits to the ability to take measurements in areas where the laser could not physically reach, such as the x cross-sections of the inboard faces of the tires.

2.2. Computational Fluid Dynamics

As indicated above, the importance of CFD in Formula One development projects has today grown to rival that of wind tunnels. The point to be observed in the use of CFD is whether the air flows around vehicles in wind tunnels and on a race track are qualitatively and quantitatively reproduced. To provide an example, this section will consider the method used when obtaining a correlation between wind tunnel and CFD results for a wake behind a tire.

The air flow around a rotating tire was elucidated in a wind tunnel using a tire and PIV measurement equipment. Figure 4 shows a vector diagram for a tire center-section obtained using PIV measurements. Here, the position of the commencement of separation from the top of the tire and the size of the wake will be focused on. (a) shows the results of PIV measurements, and (b) and (c) show CFD results. The surface mesh was approximately 1 mm, and the realizable k-ε model was used as the turbulence model. (b) shows results for y^+-1, and (c) shows results for y^+-10. y+ expresses the state of the flow as a dimensionless number calculated from the friction velocity at the nearest wall, the distance to the nearest wall, and local kinetic viscosity. For the simulation of separation, it was taken as effective to place the first mesh on the viscous sub-layer (y^+-1). The height of the first mesh for Y^+-1 was 10μm.

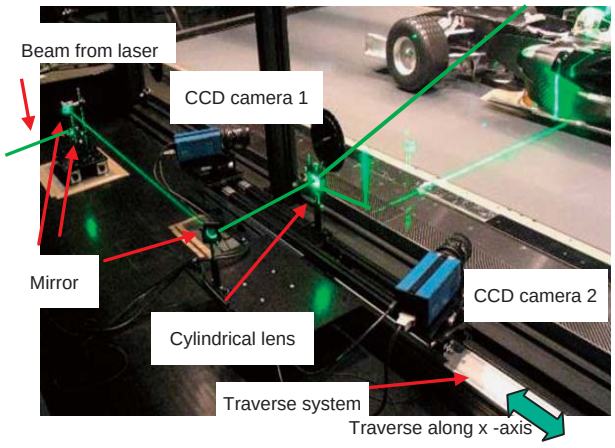

Fig. 3 PIV setting

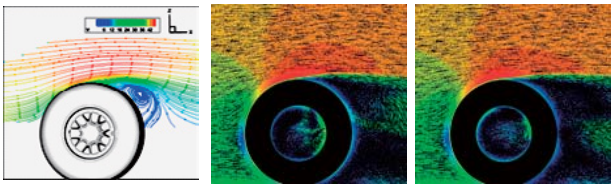

(a) PIV (b) CFDy^+ - 1 (c) CFDy^+ - 10

Fig. 4 Velocity vector at tire center section

Considering the results, (b) shows a good separation position and wake size, but the wake is excessively large in the case of (c). The result is in accord with the simulation settings in which the air speed around the tire was over-estimated.

As in the case of the tires, simulation methods for other parts were also studied, and it was decided that the following simulation methods would be used for the full-vehicle simulation:

The tetra mesh was used as the basic elements, and prisms were created from surface triangle mesh on the wings. 1 mm surface mesh was used for the airfoil sections, and 2-4 mm surface meshes were used for other parts. Figure 5 shows the mesh used for the FW. The actual first height of the boundary layer mesh was 10 μm.

Using a cocoon around the periphery of the vehicle, the surface mesh size was increased to 10 mm. Figure 6 shows an image of a cocoon. Total pressure on the cocoon was largely controlled within an overall iso-surface pressure of CpT=0.7.

In the case of the volume meshes, the mesh number differed depending on the growth rate from contiguous meshes. A growth rate of 1.7 would generate a mesh number of about 50 million, while a growth rate of 1.1 would produce a mesh number of about 300 million. Figure 7 shows the difference in space mesh density produced by a difference in the growth rate. It is clear

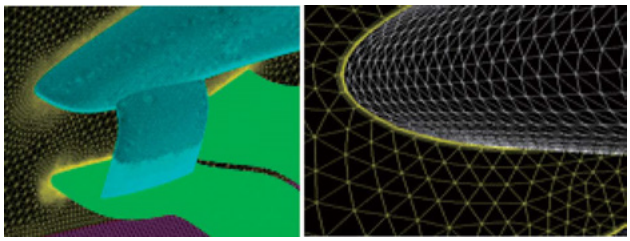

Fig. 5 Surface mesh of FW and symmetry plane

Fig. 6 Cocoon (iso-surface of CpT =0.7)

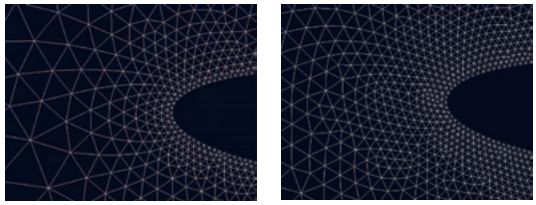

(a) Propagation 1.7 (b) Propagation 1.1

Fig. 7 Mesh propagation

that a low growth rate helps to enable a high mesh density to be maintained even in areas distant from the object.

Figure 8 shows the Cp distribution under the vehicle. It was possible to maintain a higher mesh density around the vehicle in the case of (b), which was generated using a cocoon, than was the case for (a), generated without using a cocoon. This minimized the effect of numerical diffusion and, as a result, produced strong suction. This indicates the effectiveness of using a high mesh density and conducting the simulation within the effective wave numbers.

A Linux device with a 128 GB memory was used to run PrePost. The calculation server was equipped with a 1024-core Xeon® 3.0 GHz CPU, using InfiniBand interconnects. At a growth rate of 1.1 generating 300 million meshes, 24 hours was required to converge enough for FLUENT 6.3 with 256 parallel computations.

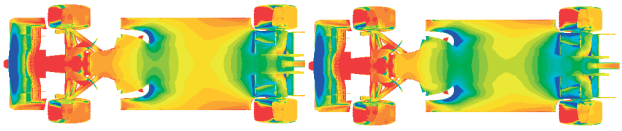

(a) Propagation 1.7 (b) Propagation 1.1

Fig. 8 Cp contour of underbody, range from -2 to 0.

3. Wind Tunnel Optimization Indices

3.1. Regulations

The major part of aerodynamics development for Formula One consists of optimization of the form of the vehicle within the scope allowed by the FIA regulations. In addition to specifying the "regulation box," the scope within which any aero parts must fit (Fig. 9), the regulations also contain a flat-bottom rule prohibiting the three-dimensional shape of the vehicle floor, a shadow rule prohibiting the use of wings and other projections that would provide ground effects in certain areas, and a rule specifying the number of RW vanes.

The regulations are also revised every few years in order to control vehicle speed increases resulting from the ongoing evolution of aerodynamics.

3.2. Ride Height Map

3.2.1. The ride height map defined

Using an advanced control logic, a simulation was conducted of the 50% model in the wind tunnel at the ride height (RH) of an actual vehicle, and aerodynamic performance was evaluated as the arithmetic mean of multiple RH. These multiple vehicle orientations form what is termed an RH map, which plays an important role in determining in what direction the vehicle can be optimized. Figure 10 shows an example of an RH map.

The most basic type of RH map is formed by selecting representative RH figures that enclose groups of RH measurements drawn from circuit data. The number of RH points per map varies with the purpose of the map. The maps used in development feature a comparatively low number of RH, while the maps used in vehicle dynamics analyses (termed "mapping data") are selected to incorporate a larger number of RH.

Using these RH maps, vehicle downforce was optimized in relation to target drag for each circuit.

3.2.2. Adding yaw (cross-winds), steer, and roll

The recent advancement in wind tunnel facilities and the associated control technologies have enabled yaw, steer, and roll to be added to the tests in addition to RH control. This has helped to enable aerodynamics development using vehicle orientations closer to actual conditions. Yaw (or cross-winds) and steer have become indispensable elements in recent aerodynamics development for Formula One, and developments are now conducted using complex vehicle orientations in a single RH map in which yaw, steer, and roll are interwoven.

3.2.3. Trajectory map and curved flow

Because the aerodynamic load on a vehicle is proportional to the square of its speed, it is sometimes thought that the only case in which aerodynamics dominates vehicle performance is that of high-speed corners taken at close to 250 km/h. However, today it is understood that the effect of aerodynamics is not insignificant even in the case of low- and medium-speed corners.

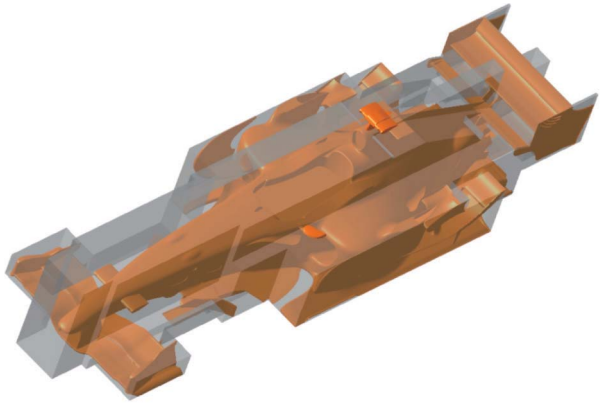

Fig. 9 Regulation box and F1 chassis

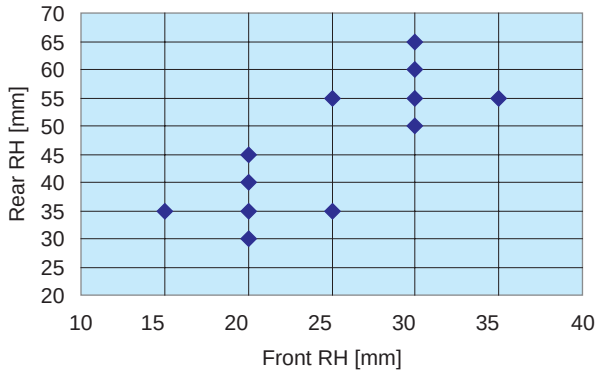

Fig. 10 Ride height map

Given this, together with the evolution of systems for controlling changes in vehicle orientation, a method of discretely reproducing a sequence of vehicle orientations linked to cornering while braking and accelerating on an RH map was developed. This is termed a trajectory map.

During actual cornering, a vehicle turns at a specific angular velocity. Because of this, the air flows at the front and rear of the vehicle have different inflow angles. The angular velocity is greater in the case of a Formula One vehicle than a normal car, and its effect therefore cannot be ignored. The difference in the front-rear inflow angle is particularly pronounced during low- and medium-speed cornering, when the angular velocity is high in relation to vehicle speed, and viewed from the perspective of a vehicle, the air flow appears bent. This is termed a curved flow (Fig. 11).

Curved flow could not, of course, be reproduced in wind tunnel tests. CFD was therefore used to investigate its effect, and the phenomenon was responded to by adding a type of yaw correction to the trajectory map.

3.2.4. Weighting and penalties

Trajectory maps functioned very well to reproduce the characteristics of specific corners, but lacked flexibility in terms of evaluation of the overall dynamic performance of the vehicle attributed to aerodynamics. In addition, the importance of minimizing shifts in the vehicle's aerodynamic center (CoP) when the vehicle orientation changes was reconfirmed from the perspective of vehicle dynamic performance.

Given this, the viable options were weighting of the RH and the application of penalties in response to shifts in the CoP. Weighting of the RH involves consideration of importance of low-, medium-, and high-speed corners, and employing a weighted means weighted towards RH corresponding to the corners where the level of contribution to lap times is higher. The application of penalties is a method of quantifying and evaluating the level of robustness to changes in vehicle orientations, in which shift of the CoP as a result of changes in vehicle orientation is considered as a reduction in effective downforce.

Even today, methods of evaluation of aerodynamic performance and the vehicle dynamic performance it generates are still being explored at the wind tunnel test stage.

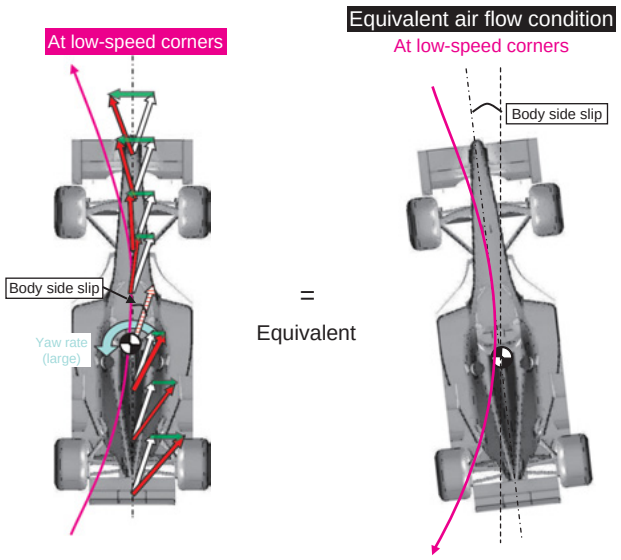

Fig. 11 Curved flow

4. Formulation of New Development Indices

This chapter will discuss the new development indices to be analyzed, the effect of tire deformation on aerodynamic load and the transient characteristics of the aerodynamic load produced on the RW during deceleration.

4.1. Effect of Tire Deformation on Aerodynamic Characteristics

When the vehicle is cornering, accelerating, or decelerating, the tires are constantly deformed due to vertical, lateral, and longitudinal forces (Fig. 12). However, the only loads that can be applied to the tires during full-scale wind tunnel tests are the vertical force from the weight of the vehicle and the aerodynamic downforce. Similarly to model-scale wind tunnel tests, it is only possible to apply vertical loads from the wheels and tires, and some side force from the belt. In other words, the deformation of the tires due to side force or longitudinal force when the vehicle is cornering, accelerating or decelerating cannot be accurately reproduced in a wind tunnel. It was therefore necessary to study the effect of tire deformation on the aerodynamic performance of the vehicle when it is actually running on a race track, and use the data obtained to formulate new indices for aerodynamics development, such as methods of reproducing tire deformation effect in a wind tunnel. This new index then enables an aerodynamically robust vehicle against tire deformation to be developed.

First, the forces acting on the tires when the vehicle is running on a track were reproduced in rig tests, and the shapes of deformed tires were obtained using three-dimensional shape measurement systems. Using these shapes, CFD was employed to analyze air flows, helping to clarify the effects of the deformed tires to the aerodynamic performance of the vehicle. Next, a method of reproducing these flows in a wind tunnel was formulated.

This chapter will focus on tire deformation due to side force, which displayed the highest level of contribution to vehicle aerodynamics.

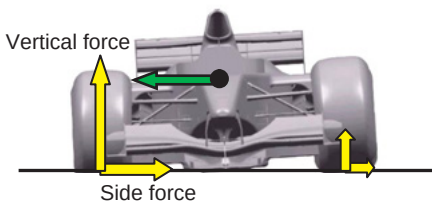

Fig. 12 Forces applied at cornering

4.1.1. Circuit data

The forces acting on the tires when the vehicle is in operation were calculated from the pushrod load and other parameters. As an example, Fig. 13 shows the side force on the left front tire during a single lap of a circuit obtained from circuit data, and Fig. 14 shows the vertical position of the tire axis resulting from the force acting on the tire. The maximum side force acting on the outer tire reaches a maximum of 10000 N, and the vertical displacement of the tire axis, i.e., the amount of vertical squash displaced by the tire, is as high as 25 mm due also to the vertical force from the downforce acting at the moment. In addition, during deceleration, a load of approximately 5000 N acts on the tire in a rearward direction.

4.1.2. Shape measurement of deformed tires

The loads acting on tires for vehicles running on track were reproduced in rig tests (Fig. 15), and the shapes of the tires were measured using three-dimensional measurement systems, including FARO, Vectron, and T-Scan. However, because these were static loads, the deformation of the tire due to centrifugal force during rotation was not reproduced. As an example, Fig. 16 shows the shape of a tire subjected to a side force of 7000 N. The side wall of the tire is deflected by approximately 20 mm in the lateral direction at close proximity to the road surface.

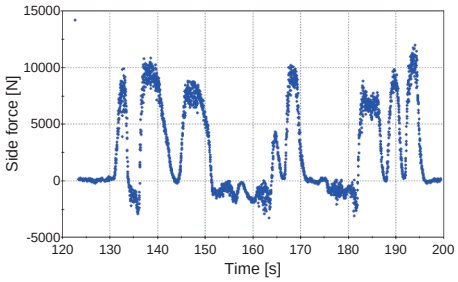

Fig. 13 Front tire side force on track

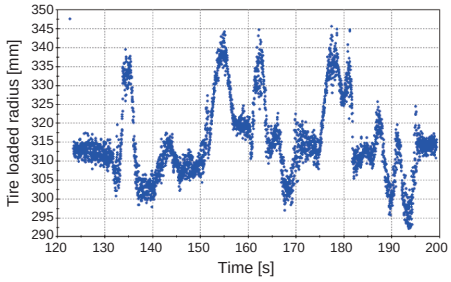

Fig. 14 Front tire loaded radius on track

Fig. 15 Tire test rig

4.1.3 Analysis of flow when front tire is deformed by side force

The measured front tire shape was analyzed using CFD. This analysis showed that, in comparison to a tire with no side force acting on it, approximately 5% of the vehicle's downforce was lost when a side force of 9000 N acted on the tire. Figure 17 shows the total pressure distribution close to the road surface with and without a side force acting on the tire. The results show that the position of the separation point on the outboard-side wall of the tire moves back significantly when a side force acts on the tire.

This backwards shift of the separation point changes the circulation around the tire in the XY planes, and the tire wake which previously flowed to the outboard of the vehicle now flows under the vehicle (Fig. 18). The fact that this reduces the dynamic pressure underneath the

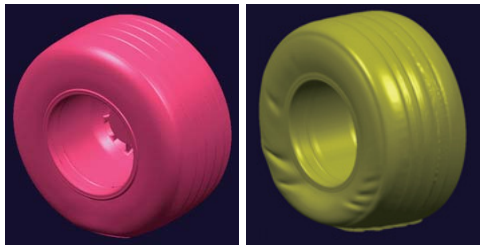

(a) Baseline (b) Fy: 7000 N

Fig. 16 Snapshots of scanned tire

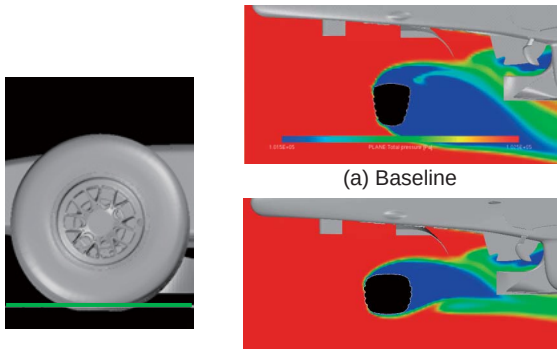

(a) Baseline

(b) Fy: 9000 N

Fig. 17 Total pressure distribution

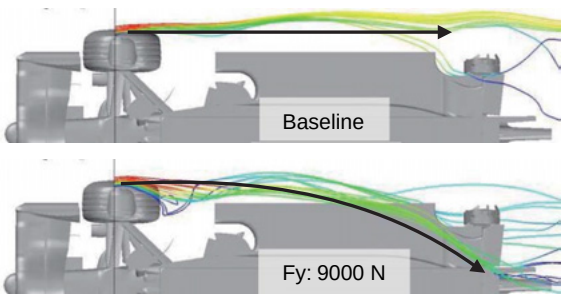

Fig. 18 Tire wake direction

vehicle, resulting in a decline in downforce, can be seen from the change in the static pressure underneath the vehicle when the tire goes from a state of no side force to one in which side force is acting (Fig. 19).

Next, the reason for the shift of the separation point was analyzed. First, a simulation was conducted to apply the surface form of a tire with no side force acting on it to outboard side of a tire with a side force applied (Fig. 20). The resulting forward shift of the separation point resulted in a recovery of 4% of the 5% loss in downforce.

Next, the shape of the tire contact patch was focused on, and a simulation was conducted with an edge applied to the corner of the leading edge of the outboard side of the tire with a side force applied (Fig. 21). In this case, 4.5% of the downforce was recovered as well, producing a result almost identical to that for a tire with no side force acting on it.

Next, this phenomenon was reproduced using a 50% model in a wind tunnel. However, because side force cannot be applied to the tires in a wind tunnel, at first only the vertical displacement was reproduced.

Figure 22 shows the results of measurement taken using two-component PIV. As in the case of the CFD results, the deformation of the tire resulted in the backwards shift of the separation point on the outboard-side wall of the tire. It also showed 3% loss of downforce, which agrees with the CFD results qualitatively as well.

Despite differences in the exact shape of tire deformation, both CFD and wind tunnel results showed that the deformation of the tires produces a backwards shift of the separation point, which causes the loss of downforce on the vehicle.

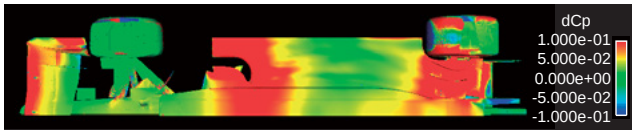

Fig. 19 Deformed tire effect (delta Cp)

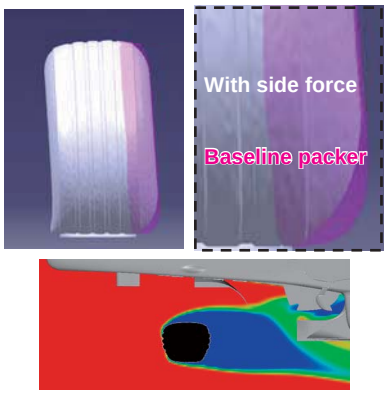

Fig. 20 Result of baseline packer

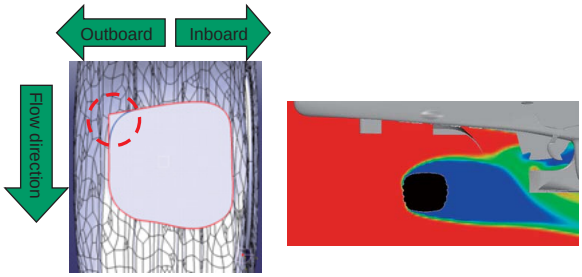

Fig. 21 Result of edged contact patch corner

4.1.4. Analysis of flow when rear tire is deformed by side force

CFD was used to conduct an analysis for the rear tires in the same way as previously conducted for the front tires. The results showed that approximately 4% of the vehicle's downforce was lost when a side force of 6500 N was applied, as compared to a state in which no side force was applied. Figure 23 compares the total

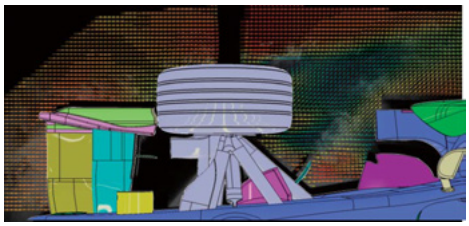

(a) Baseline

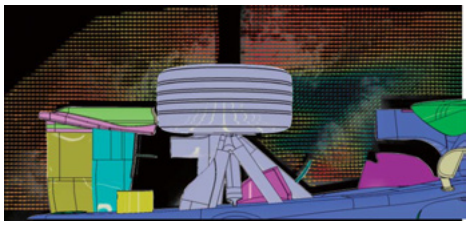

(b) 10mm squashed

Fig. 22 PIV velocity vector

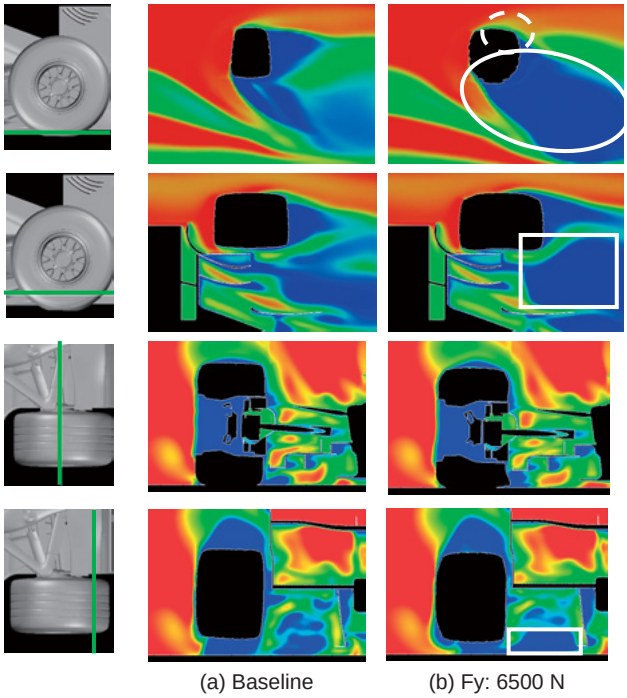

(a) Baseline (b) Fy: 6500 N

Fig. 23 Tire wake comparison (total pressure)

pressure distribution close to the diffuser for tires with no side force and a side force of 6500 N. When the side force is applied, the separation area of the inner side of the tire becomes large (shown by the solid circle in the figure), simultaneously, as was the case for the front tire, the separation point shifts to the rear (shown by the broken circle in the figure), and the wake of the tire flows to the center of the vehicle (shown by the solid square in the figure). The fact that this becomes a blockage and results in the decline of the diffuser flow, with a consequent decline in the vehicle's downforce, can be judged from the change in the static pressure underneath the vehicle when the tire goes from a state of no side force to one in which side force is applied (Fig. 24).

4.1.5. Verification of effect using full-scale wind tunnel tests

The results obtained from CFD and model-scale wind tunnel tests were verified using an actual vehicle in the wind tunnel. Due to the system limitations of the wind tunnel, it is impossible to apply any loads to the tires other than the weight of the vehicle and the downforce. Therefore, changes in the downforce produced by changes in wind speed were used to vary the amount of squash of the tires in the vertical direction, the effect of which was analyzed. At this time, RH was adjusted by varying the length of the push rods.

Figure 25 shows the amount of squashing of the front tires and the rate of change of normalized downforce against wind speed. The downforce at a wind speed of 30 m/s was employed as the standard for the rate of change of downforce. Normalized downforce declines with the squashing of the tires as the downforce increases with increasing wind speed. This matches the tendency of results from CFD and the model-scale wind tunnel tests, as discussed in Section 4.1.3. In addition, PIV confirmed that this change in the normalized downforce occurred with the shift of the separation point on the outboard side of the tire.

Figure 26 shows the shape of a front tire when the downforces generated at vehicle speeds of 40 m/s and 70 m/s were statically loaded on it. The results show that the increase in load relaxes the apex of the outboard side of the contact patch, and increases the degree of deformation of the bottom of the tire.

However, in addition to the effect of the deformation of the tires, the effects of deflection of bodywork due to wind and variations in the position of the suspension arms are also included in the changes in the downforce, and these effects, however small they may be, need to be taken into account.

4.1.6. Effect of differences between tire manufacturers

The shape of the deflection of the side of the tire and the shape of the contact patch also differ between tire manufacturers, and the effects of these parameters therefore also differ. For example, if tires manufactured by maker A and maker B which display an identical amount of squashing are compared using CFD, the vehicle downforce when maker B's tires are used will be approximately 5% lower. As Fig. 27 shows, this is because the separation point on the outboard of maker B's front tires shifts rearward, and the wakes from the inner sides of the maker's rear tires are large. This tendency matches the changes in magnitude of the normalized downforce in the full-scale wind tunnel tests

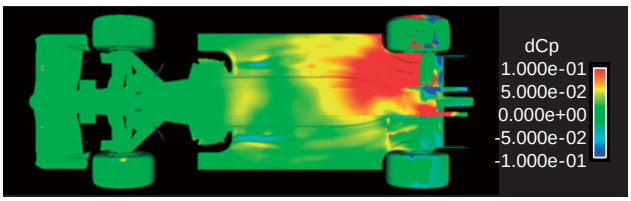

Fig. 24 Deformed tire effect (delta Cp)

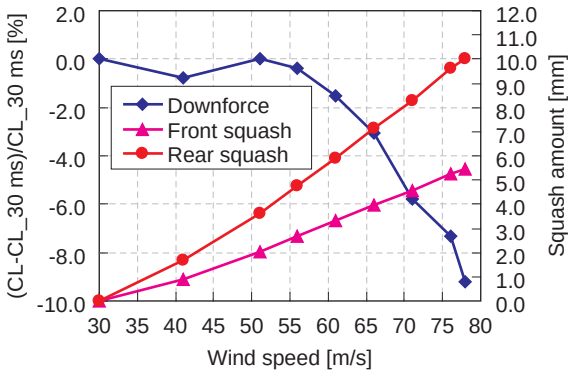

Fig. 25 Squash and downforce change

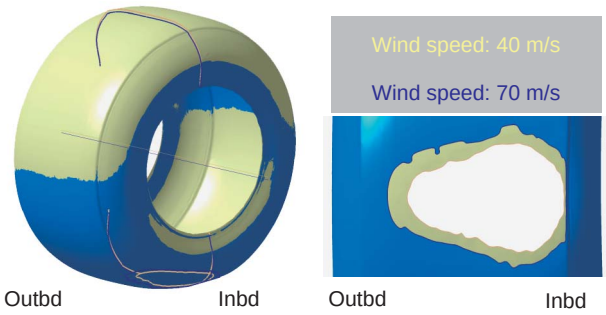

Fig. 26 Snapshot of scanned tire

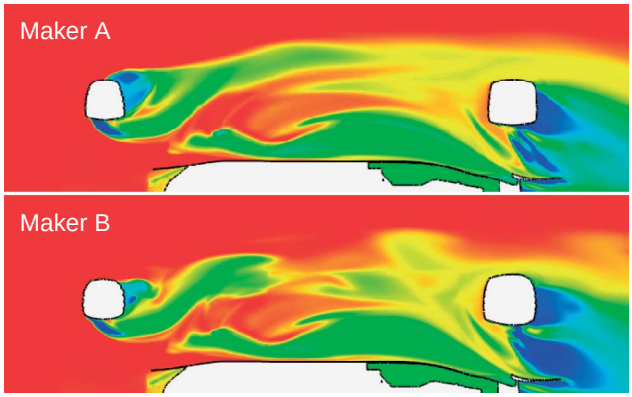

Fig. 27 Total pressure under floor

(Fig. 28). However, because the shape of the contact patch also changes with the camber and other parameters, a conclusion cannot be drawn until these other factors are taken into consideration.

4.1.7. Methods of reproducing tire deflection in wind tunnel

In order to obtain stable aerodynamic performance on the track, it was necessary to increase robustness against tire deformation. This made it necessary to reproduce worst-case scenarios in wind tunnel development. It was considered that using the pushrods to apply vertical loads to the tire, or, as shown in Fig. 29, using a roller to push the side wall from the inner side of the tire, would be effective methods of doing so.

4.2. Transient Aerodynamic Characteristics during Deceleration

Data obtained during track test had indicated the possibility that normalized downforce declined when the vehicle was decelerating. In particular, it was possible that the normalized downforce was declining because of the development of a boundary layer at the RW due to deceleration and the fact that the RW wake overtook it. An actual RW was therefore used in slow-motion tests in a water towing tank, and the occurrence or non-occurrence of separation and the changes in load when the vehicle was decelerating were analyzed.

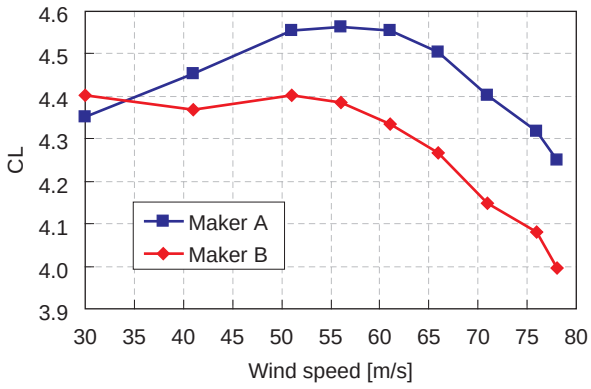

Fig. 28 Normalized downforce comparison

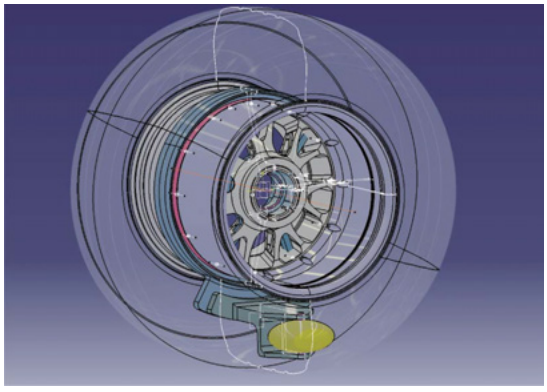

Fig. 29 Method of deforming rubber tire in wind tunnel

4.2.1. Test conditions

First, in order to make non-aerodynamic factors such as deformation of the RW under loads correspond to conditions when the vehicle was actually running on a race track, the aerodynamic loads in a towing tank and that on a track were coordinated. If the forces in air and in water are coordinated, i.e., the dynamic pressure is made constant,

$$q = \frac{1}{2}\rho U^2 = const$$

where ρ: density and U: speed,

then at an atmospheric temperature of 25˚C and a water temperature of 15˚C, the speed in water will be

$$U_{water} = \sqrt{\frac{\rho_{air}}{\rho_{water}}} U_{air} = 0.034 U_{air}$$

i.e., the speed in water will be one-thirtieth of that in air. The Reynolds number at this time is given by

$$\mathrm{Re}_{water} = \frac{U_{water}\nu_{air}}{U_{air}\nu_{water}} \mathrm{Re}_{air} = 0.47\ \mathrm{Re}_{air}$$

where ν: dynamic viscosity coefficient. The Reynolds number in water is half its value in air, but considering changes in vehicle speed and the results of model-scale wind tunnel tests, this was in an allowable range.

When the Froude number is made constant,

$$Fr = \frac{U^2}{gL} = const$$

where g: acceleration and L: reference length, the acceleration in water is expressed by

$$g_{water} = \frac{U^2_{water}}{U^2_{air}} g_{air} = 0.0012 g_{air}$$

i.e., acceleration in water is 1/1000 of that in air.

Given this, it is possible to conduct slow-motion tests in water, and transient aerodynamic loads during deceleration, which are challenging to measure when the vehicle is actually running on a race track due to error factors, can be measured with a high degree of accuracy. During this program of tests, deceleration tests from 0.005-0.05 G and fixed-speed tests from 1.02-2.94 m/s (corresponding to 106-307 km/h in air) were conducted.

4.2.2. Towing tank and test rig

The towing tank employed in the tests was 200 m long, 10 m wide, and 5 m deep (Fig. 30). A six-

Fig. 30 Towing tank

component load cell and a mounting rig were attached to the towing train, and the RW was positioned upside-down in 1 m of water. To help prevent waves from being generated on the surface of the water, an acrylic plate was positioned close to the surface (Fig. 31).

4.2.3. Test results

In order to investigate the existence of transient aerodynamic characteristics during deceleration, the RW downforce when decelerating from 2.94 m/s (corresponding to 307 km/h in air) at 0.005 G (corresponding to 4.2 G in air) was compared with values for driving at a constant speed (Fig. 32). The same tests were conducted with braking G-force varied down to 0.05 G. No transient characteristics during deceleration were observed during these tests, verifying that the RW was fulfilling its function as a unit according to design targets even when the vehicle was decelerating.

The result indicated that towing tank tests were an effective method of verifying performance on a track when, for example, dealing with higher-load RW or studying aeroelasticity. In addition, the towing tank was an effective means of reproducing new fluid phenomena, such as when studying the possibility of a decline in the normalized RW downforce during deceleration due to the rear-tire wakes overtaking the RW.

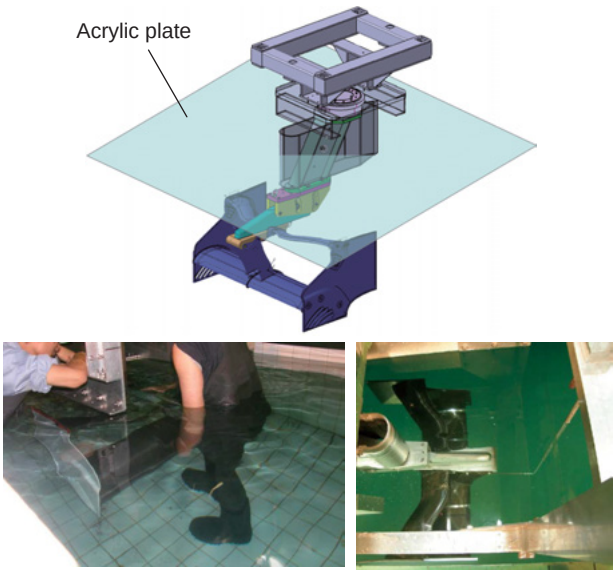

Fig. 31 RW assembly

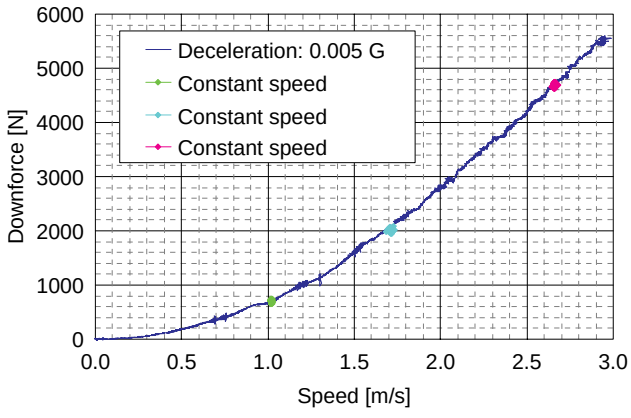

Fig. 32 Hydrodynamic force comparison between deceleration and constant speed modes

5. Afterword

This paper has discussed aerodynamics development indices used until 2008, and new indices such as the analysis of the effect of tire deformation on aerodynamic loads and the analysis of transient aerodynamic characteristics during deceleration. These efforts deepened understanding of the air flow around the vehicle actually running on a race track.

Acknowledgments

The authors wish to take this opportunity to offer their sincere thanks to all the staff members of the former BAR and HRF1 for their many years of assistance in aerodynamics developments, and also to the staff of IHI Corporation who generously offered their advice and assistance in the towing tank tests.

■ Author ■


Atsushi OGAWA


Shujiro YANO


Susumu MASHIO


Takashi TAKIGUCHI


Shinsuke NAKAMURA

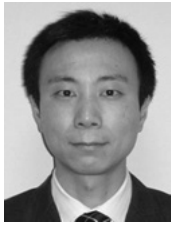
Mitsuru SHINGAI